

A HOT COCOON IN THE ULTRALONG GRB 130925A: HINTS OF A POPIII-LIKE PROGENITOR IN A LOW DENSITY WIND ENVIRONMENT

LUIGI PIRO¹, ELEONORA TROJA², BRUCE GENDRE³, GABRIELE GHISELLINI⁴, ROBERTO RICCI⁵, KEITH BANNISTER^{6,7},
 FABRIZIO FIORE⁸, LAUREN A. KIDD², SILVIA PIRANOMONTE⁸, MARK H. WIERINGA⁹

Draft version June 24, 2014

ABSTRACT

GRB 130925A is a peculiar event characterized by an extremely long gamma-ray duration (≈ 7 ks), as well as dramatic flaring in the X-rays for ≈ 20 ks. After this period, its X-ray afterglow shows an atypical soft spectrum with photon index $\Gamma \sim 4$, as observed by *Swift* and *Chandra*, until $\approx 10^7$ s, when *XMM-Newton* observations uncover a harder spectral shape with $\Gamma \sim 2.5$, commonly observed in GRB afterglows. We find that two distinct emission components are needed to explain the X-ray observations: a thermal component, which dominates the X-ray emission for several weeks, and a non-thermal component, consistent with a typical afterglow. A forward shock model well describes the broadband (from radio to X-rays) afterglow spectrum at various epochs. It requires an ambient medium with a very low density wind profile, consistent with that expected from a low-metallicity blue supergiant (BSG). The thermal component has a remarkably constant size and a total energy consistent with those expected by a hot cocoon surrounding the relativistic jet. We argue that the features observed in this GRB (its ultralong duration, the thermal cocoon, and the low density wind environment) are associated with a low metallicity BSG progenitor and, thus, should characterize the class of ultralong GRBs.

Subject headings: gamma-ray burst: individual (GRB130925A) – stars: Population III

1. INTRODUCTION

Gamma-ray bursts (GRBs) are traditionally divided into two classes based on the properties of the observed gamma-ray emission: short duration (< 2 s) hard spectrum and long duration (> 2 s) soft spectrum bursts (Kouveliotou et al. 1993). Between 2010 and 2012, the *Swift* mission (Gehrels et al. 2004) discovered three unusually long-lasting stellar explosions that could represent a previously unrecognized class of high-energy transients. These events, dubbed ultra-long GRBs, persist for hours, a period up to 100 times longer than typical GRBs. Gendre et al. (2013) proposed that their unusual long duration may reflect the physical size of their stellar progenitor, likely a low-metallicity blue supergiant (BSG). This scenario is favored because the associated low mass loss rate retains the outer stellar layers, that can then continuously supply mass to the central engine over a duration of $> 10,000$ s. In fact, accretion timescales can be crudely estimated as the free-fall time of the external layers (Kumar et al. 2008; Quataert & Kasen 2012), $t_{ff} \approx 10^4 R_{12}^{3/2} M_{50}^{-1/2}$ s, where

the mass $M = 50 M_{50} M_{\odot}$, and radius $R = 10^{12} R_{12}$ cm are typical of a BSG with low metallicity (Heger et al. 2003; Woosley & Heger 2012). The lack of any bright supernova component (Levan et al. 2014) further supports the idea of a progenitor system different from the compact Wolf-Rayet (WR) star, which gives birth to standard long GRBs (Woosley & Bloom 2006).

In the scenario proposed by Gendre et al. (2013), ultra-long GRBs could represent the closest link ever discovered between GRBs and the rare Population III stars (Abel et al. 2002; Bromm et al. 2002), which end their lives as BSGs with massive hydrogen envelopes (Woosley et al. 2002). Ultra-long GRBs in the local Universe offer us the unique opportunity to study the explosion mechanisms of the most distant stellar explosions (Mészáros & Rees 2010; Suwa & Ioka 2011): those happening during the ‘Cosmic Dawn’ (Barkana & Loeb 2001).

In this Letter, we present the results of our X-ray and radio monitoring campaign of the recently discovered ultra-long GRB 130925A. Besides its extreme long gamma-ray duration (≈ 7 ks), this event was also characterized by an unusually soft X-ray spectrum during its afterglow phase, accompanied by a hard-to-soft-to-hard spectral evolution in time. Contrary to previous works, we argue that the atypical afterglow behavior of this ultra-long GRB is closely related to its atypical stellar progenitor.

2. DATA ANALYSIS

2.1. Observations and data reduction

GRB 130925A triggered the *Swift* Burst Alert Telescope (BAT) on 2013 September 25 at 04:11:24 UT, which we refer to as T_0 . Its prompt gamma-ray phase was also detected at earlier times by *INTEGRAL* at T_0 .

¹ INAF- Istituto Astrofisica e Planetologia Spaziali, Via Fosso Cavaliere 100, I-00133, Rome, Italy

² NASA/GSFC, Greenbelt, MD 20771, USA

³ ARTEMIS, UMR 7250, Boulevard de l’ Observatoire, Nice, Cedex 4, France

⁴ INAF-Osservatorio Astronomico di Brera, via E. Bianchi 46, I-23807 Merate (LC), Italy

⁵ (INAF-Istituto di Radioastronomia, Via Gobetti 101, I-40129 Bologna, Italy

⁶ CSIRO Astronomy and Space Science, Marsfield NSW 2122, Australia

⁷ Bolton Fellow

⁸ INAF-Osservatorio Astronomico di Roma, via Frascati 33, I-00040 Monteporzio Catone (RM), Italy

⁹ CSIRO Astronomy and Space Science, Locked Bag 194, NSW 2390, Narrabri, Australia

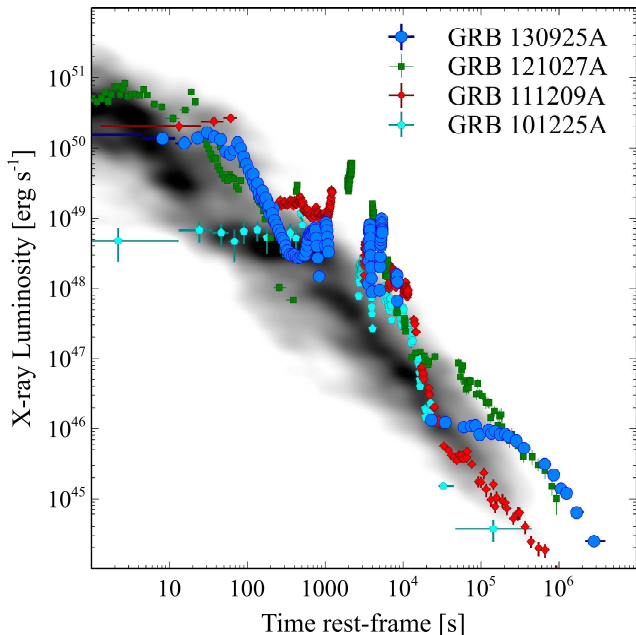


Figure 1. X-ray luminosity light curves for ultra-long GRBs: GRB101225A at $z=0.84$, GRB111209A at $z=0.67$, GRB121027A at $z=1.773$ and GRB 130925A at $z=0.35$. The gray area shows the light curves of ~ 200 *Swift* long GRBs with measured redshift. The canonical (steep-flat-normal) afterglow decay can be recognized. Ultra-long GRBs display continuous prompt emission activity up to late times, when standard long GRBs already follow the “normal” afterglow decay phase.

718 s (Savchenko et al. 2013), by the *Fermi* Gamma-Ray Burst Monitor at T_0+15 m (Fitzpatrick 2013), and by Konus-Wind (Golenetskii et al. 2013). The GRB emission showed several strong bursts visible by BAT up to ≈ 7 ks, as observed in other ultra-long GRBs. A comparison between GRB 130925A, ultra-long GRBs, and long GRBs is shown in Fig.1.

Pointed observations with the *Swift* X-ray Telescope (XRT) began at T_0+151 s, revealing a bright and highly variable X-ray afterglow. Strong flaring episodes were detected until T_0+6 hrs, after which the afterglow exhibited a smooth power-law decay (Fig.1). Follow-up observations with the XRT lasted for ~ 6 months, for a total net exposure of 425 ks in Photon Counting mode. XRT data were processed using the XRT Data Analysis Software (XRTDAS; ver. 12.9.3) distributed within HEASOFT. We used the latest release of the XRT Calibration Database and followed a standard reduction procedure (see Evans et al. 2009). We also analyze a *Chandra* observation (PI: E. Bellm, see Bellm et al. 2014), performed at T_0+11 days, for a total net exposure of 44 ks. *Chandra* data were reduced with the CIAO v.4.6 and the relevant calibration files.

In order to characterize the late-time afterglow evolution, a dedicated Target of Opportunity observation with *XMM-Newton* (PI: L. Piro) was carried out on December 26 ($T_0 + 3$ months) for 100 ks. *XMM* data were reduced using SAS version 13.5.0. After applying standard filtering criteria and removing time intervals with high flaring background activity, the total net exposure is 85 ks.

The optical/IR counterpart of GRB 130925A was detected by GROND (Sudilovsky et al. 2013), and later

localized by the HST to lie $0.12''$ from the galaxy nucleus (Tanvir et al. 2013). The red and relatively faint afterglow suggests that GRB 130925A was a highly extinguished event. Spectroscopic observations of the underlying host galaxy measured a redshift $z=0.347$ (Vreeswijk et al. 2013).

Radio observations with the Australia Telescope Compact Array (ATCA) detected a source at a position consistent with the X-ray and optical localizations. These observations were carried out into three campaigns: one in October 2013 (Bannister et al. 2013), one in January 2014, and one in February 2014 (PI: L. Piro). Radio data were calibrated and imaged using standard procedures within the MIRIAD data reduction package (Sault et al. 1995).

2.2. X-rays

A detailed analysis of the early X-ray flares is presented in Evans et al. (2014); here we focus on the late (>20 ks) afterglow emission. The X-ray emission in the 0.3-10 keV energy band decays as a simple power-law function, $f_X \propto t^{-\alpha}$, with slope $\alpha=0.82$, steepening to $\alpha=1.32$ after ~ 300 ks. The hardness ratio light curve displays significant variations up to late times, which is unusual for standard GRB afterglows. In order to quantify the spectral evolution, we performed a time-resolved spectral analysis using XSPEC v.12.8.1 (Arnaud 1996). Our results are summarized in Table 1 (spectra A1-A6). The X-ray spectra were described by an absorbed power-law model. The Galactic absorption component was kept fixed at the value of $1.66 \times 10^{20} \text{ cm}^{-2}$. A redshifted absorption component, modeling the host intrinsic absorption, was initially left free to vary. The afterglow spectrum shows a hard-to-soft (from $\Gamma \sim 3.5$ to ~ 4.6) followed by a soft-to-hard (from $\Gamma \sim 4.6$ to ~ 2.5) evolution. The spectral fits, although acceptable, yield unphysical variations of the absorbing column, correlated with the evolution of the power-law index (Table 1, col. 2-3). We, therefore, linked the intrinsic absorption between the different spectra (Table 1, col. 4-6). The resulting fit is poor ($\chi^2=552$ for 429 dof), mainly because the soft power-law spectrum underestimates the flux above ~ 3 keV.

A steep non-thermal spectrum ($3.3 < \Gamma < 4.4$) is atypical in GRB afterglows, and is generally seen as an indication of a thermal component which, over the limited 0.3-10 keV energy bandpass, cannot be fully resolved. Each spectrum was then fit by adding a black body component to the simple non-thermal power-law. The improvement of χ^2 is highly significant. However, despite the good statistics of the *Swift* and *Chandra* spectra, the spectral parameters were not well constrained, with an error range that included the blackbody temperatures and spectral indices found by Bellm et al. (2014). This is mainly because the flux of the blackbody component is comparable to, or even larger than, the power-law flux and dominates the emission below 3 keV.

In this respect, the late *XMM* observation was crucial to constrain the model. The high throughput of the telescope allowed us to gather enough counts at late times, when the thermal component had shifted to lower temperatures, and the two emission components could be better disentangled. The *XMM* spectrum can be described by a power law with $\Gamma = 2.50 \pm 0.10$, rather common in GRB afterglows. The blackbody component

Table 1
Results of the spectral fits^a

Time interval	Power Law		Power Law (N_H linked)			Power Law (N_H and Γ linked)+ Black Body					
	N_H	Γ	N_H	Γ	χ^2/dof	N_H	Γ	kT_{BB}	L_{BB}^{BB}	R_{BB}^{BB}	χ^2/dof
E1: 150-500 s	$1.36^{+0.05}_{-0.05}$	$1.72^{+0.03}_{-0.03}$	$1.38^{+0.05}_{-0.05}$	$1.73^{+0.03}_{-0.03}$	852/820	$1.80^{+0.15}_{-0.15}$	$1.73^{+0.05}_{-0.08}$	$1.4^{+0.3}_{-0.3}$	$2.4^{+0.9}_{-0.9} \times 10^3$	1.2 ± 0.6	806/817
E2: 500-700 s	$1.50^{+0.10}_{-0.10}$	$1.71^{+0.06}_{-0.06}$	—	$1.67^{+0.04}_{-0.04}$	—	—	—	$1.30^{+0.15}_{-0.15}$	$2.6^{+0.6}_{-0.6} \times 10^3$	1.4 ± 0.3	—
E3: 1150-1340 s	$1.40^{+0.10}_{-0.10}$	$1.9^{+0.10}_{-0.10}$	$1.40^{+0.10}_{-0.10}$	$1.9^{+0.10}_{-0.10}$	71/83	$1.4^{+0.2}_{-0.2}$	$2.1^{+0.3}_{-0.3}$	$1.5^{+0.6}_{-0.6}$	$7^{+7}_{-7} \times 10^2$	0.6 ± 0.6	65/81
A1: 20-300 ks	$2.30^{+0.10}_{-0.10}$	$3.5^{+0.06}_{-0.06}$	$2.10^{+0.10}_{-0.10}$	$3.4^{+0.10}_{-0.10}$	552/429	$1.40^{+0.10}_{-0.10}$	$2.4^{+0.2}_{-0.2}$	$0.5^{+0.03}_{-0.03}$	23 ± 3	1.00 ± 0.10	471/422
A2: 300-700 ks	$2.7^{+0.2}_{-0.2}$	$4.6^{+0.2}_{-0.2}$	—	$4.10^{+0.10}_{-0.10}$	—	—	—	$0.45^{+0.03}_{-0.03}$	10.0 ± 1.0	0.90 ± 0.10	—
A3: 0.7-2 Ms	$1.9^{+0.2}_{-0.2}$	$4.0^{+0.2}_{-0.2}$	—	$4.2^{+0.2}_{-0.2}$	—	—	—	$0.34^{+0.04}_{-0.04}$	4.2 ± 0.8	0.9 ± 0.2	—
A4 ^b : 0.95-1 Ms	$1.90^{+0.10}_{-0.10}$	$3.80^{+0.10}_{-0.10}$	—	$4.0^{+0.10}_{-0.10}$	—	—	—	$0.35^{+0.03}_{-0.03}$	3.4 ± 0.4	0.80 ± 0.10	—
A5: 3-8 Ms	$1.3^{+0.4}_{-0.4}$	$3.0^{+0.4}_{-0.4}$	—	$3.8^{+0.5}_{-0.5}$	—	—	—	$0.30^{+0.10}_{-0.10}$	0.3 ± 0.2	$0.4^{+0.6}_{-0.3}$	—
A6 ^c : 0.78-8 Ms	$1.10^{+0.14}_{-0.14}$	$2.50^{+0.10}_{-0.10}$	—	$3.5^{+0.2}_{-0.2}$	—	—	—	$0.23^{+0.05}_{-0.05}$	0.17 ± 0.10	0.4 ± 0.3	—

^aNOTES: For the power-law model, we report the absorbing column N_H in units of 10^{22} cm^{-2} , and the photon index Γ . For the blackbody model, we report the black-body temperature kT_{BB} in units of keV, luminosity L_{BB} in units of $10^{44} \text{ ergs}^{-1}$, and radius R_{BB} in units of 10^{11} cm .

^bChandra

^cXMM-Newton

is still significantly detected ($\Delta\chi^2=15.3$ corresponding to a chance probability of 6.8×10^{-4}) with temperature $kT = 0.25 \pm 0.04 \text{ keV}$.

Based on these results, we tested whether the observed X-ray emission could be described by an underlying non-thermal afterglow, and a dominating, highly variable thermal component. The spectra were simultaneously fit by linking the absorbing column and the power-law photon index, and by letting the black-body parameters free to vary (Table 1, col. 7-12). Compared to the reference model (col. 4-6), the addition of the blackbody improves the fit at a very high level, yielding a $\Delta\chi^2=81$ for 7 additional parameters corresponding to a chance probability of $< 10^{-8}$.

Motivated by the results derived at $t \gtrsim 20 \text{ ks}$, we also searched for a thermal component at earlier times, excluding the periods dominated by the X-ray flares. The results are reported in Table 1 (spectra E1-E3). The early-time spectra are dominated by the non-thermal emission, but consistent with the presence of a black body component with temperature $kT_{BB} \approx 1 \text{ keV}$.

2.3. Radio

The full set of ATCA measurements is listed in Table 2. Flux densities and corresponding 1σ errors were obtained from the task *maxfit* in MIRIAD. In the first two campaigns (October 2013, and January 2014) the source was localized with typical uncertainty of $0.9\text{-}1.3''$.

Table 2
Radio observations of GRB 130925A

Date	5.5 GHz	9 GHz	17 GHz	19 GHz
	[μJy]	[μJy]	[μJy]	[μJy]
Oct 09, 2013	—	161 ± 24	146 ± 22	109 ± 28
Oct 14, 2013	—	162 ± 19	—	—
Oct 15, 2013	—	—	170 ± 31	169 ± 43
Jan 04, 2014	165 ± 31	245 ± 30	58 ± 18	175 ± 19

To further improve the positional accuracy of the target, another 17 and 19-GHz follow-up was carried out in February 2014 with the ATCA in its most extended array configuration (6D: maximum baseline length 6 km). Notwithstanding poor observing conditions we were able to obtain a weak ($S/N=3.3$) detection of the target at 17 GHz. The best positional accuracy was obtained by fitting a 2-D Gaussian model to the target image at 17 GHz with the MIRIAD task *imfit*. The resulting position is: RA=02:44:42.949, Dec=-26:09:11.090 with (1σ) errors $\Delta\text{RA}=0.106''$, and $\Delta\text{Dec}=0.621''$.

The radio source remains nearly constant in brightness (within the uncertainties) over a period of ~ 4 months. A comparison with the HST images, which we downloaded from the public archive, shows that the radio position is consistent with the faint transient reported by Tanvir et al. (2013) and offset from the galaxy nucleus. The probability of a chance alignment for a source this brightness is negligible ($P \approx 3 \times 10^{-5}$), and we conclude that the radio source is the GRB afterglow. Its relatively constant flux suggests that the blastwave is expanding into a circumburst medium with a wind-like density profile, $\rho(r) \propto r^{-2}$.

3. DISCUSSION

Two salient features characterize GRB 130925A: an extreme long duration, and a very steep X-ray spectrum. As shown in Figure 1, an intense and persistent flaring activity dominates the emission for the first six hours while, over this period, typical long GRBs already entered the normal afterglow phase. After the flaring ceases, the X-ray emission displays an unusually steep spectrum. The scenario that we have tested envisions the presence of two components contributing to the X-ray emission: a thermal component, well described by a black body emission with constant radius, decreasing temperature and luminosity; and an underlying non-thermal component. In the following we discuss their properties, and their possible origin.

3.1. External shock into a low-density wind environment

The non-thermal emission is well-described by a power-law with spectral slope $\beta = \Gamma - 1 = 1.4 \pm 0.2$, consistent with the spectral indices observed in GRB afterglows (de Pasquale et al. 2006; Willingale et al. 2007). The X-ray light curve above 3 keV (inset of Fig. 2), where the non-thermal component dominates, shows a power-law temporal decay with $\alpha = 1.20 \pm 0.05$, consistent with the closure relation $\alpha = (3\beta - 1)/2$ for $\nu_X > \nu_c$. This evidence motivated us in modelling the X-ray non-thermal component and the radio data with a standard forward shock model (Granot & Sari 2002). The broad band spectra from radio to X-rays at three epochs were fitted simultaneously, yielding a good agreement with a forward shock expanding in a wind-like environment. The best fit model and parameters are presented in Fig. 2. The blastwave energy $E_k \approx 10^{53}$ erg is comparable to the observed gamma-ray energy $E_{\gamma,iso} \approx 1.5 \times 10^{53}$ erg, which implies a high radiative efficiency of the prompt emission mechanism. The tenuous, wind driven medium derived from the fit implies a low mass loss rate of $\dot{M} \approx 3.6 \times 10^{-8} M_\odot \text{ yr}^{-1}$ for a wind velocity of $v_w = 10^3 \text{ km s}^{-1}$, consistent with a very low-metallicity BSG progenitor (Vink et al. 2001; Kudritzki 2002). From the lack of jet-break signature in the 3-10 keV light curve, we derive a lower limit on the jet-break time $t_j \gtrsim 90 \text{ d}$, and a jet opening angle $\theta_j \gtrsim 2 \text{ deg}$.

3.2. A hot cocoon

The luminosity, temperature, and apparent radius of the blackbody component are plotted in Fig. 3 as functions of time. The luminosity declines as $L_{BB} \propto t^{-0.9}$, while the temperature exhibits a slower decreasing trend, $T \propto t^{-0.2}$. The apparent radius is $R_{BB} \approx 10^{11} \text{ cm}$, showing that, within the uncertainties, the size of the emitting source remained remarkably constant in spite of the large variation in luminosity.

Three main mechanisms can produce a thermal component in GRBs, namely a shock break out, the jet photosphere, and a hot cocoon. Shock breakouts are characterized by durations $\ll 10,000 \text{ s}$ and peak X-ray luminosities from $\approx 10^{44} \text{ erg s}^{-1}$ to $10^{46} \text{ erg s}^{-1}$ (Ensmann & Burrows 1992; Campana et al. 2006), not consistent with the long timescale and large luminosity observed in GRB 130925A.

Bright thermal emission from the fireball photosphere may emerge during the prompt gamma-ray phase. This high energy photospheric component is associated to the optically thick plasma of a relativistic jet, and decays in luminosity and temperature as a power-law in time (Ryde & Pe'er 2009). It may still be detectable in the soft X-rays a few hundreds seconds after the burst (Sparre & Starling 2012; Friis & Watson 2013) and, in principle, can continue on much longer time scales if the jet continues to be powered. Wong et al. (2014) showed that for a BSG this can be indeed the case: the fall-back of the external layers onto the central black hole yields an accretion rate $\dot{M} \approx 10 \text{ t}^{-5/3} M_\odot \text{ yr}^{-1}$, and a corresponding jet luminosity $L_{jet} \approx 2 \times 10^{49} \eta_{-1} t_3^{-5/3} \text{ erg s}^{-1}$. Here $\eta = 0.1 \eta_{-1}$ is the mass to energy conversion efficiency, and $t = 1000 t_3 \text{ s}$. The photospheric radius is $r_{ph} = 5.8 \times 10^{11} L_{jet,51} \Gamma_2^{-3} \text{ cm}$ (Abramowicz et al. 1991; Pe'er et al. 2012), where $\Gamma = 100 \Gamma_2$ is the jet Lorentz factor. Therefore, a photospheric emission with constant

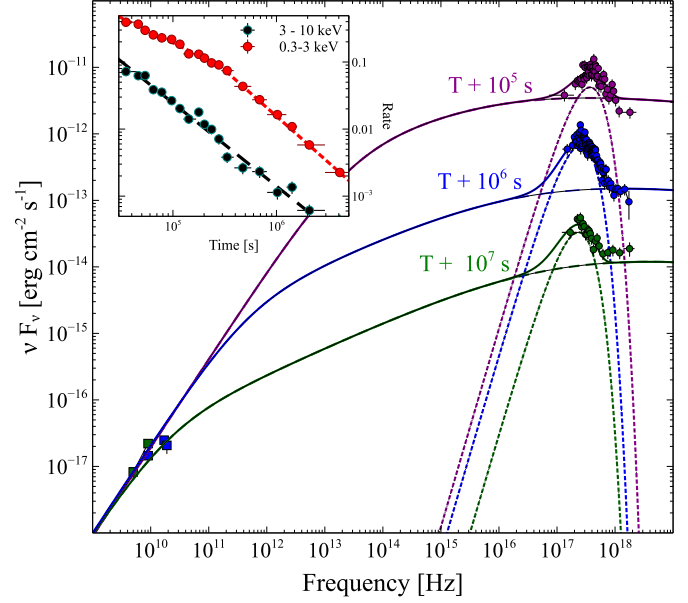


Figure 2. Broadband afterglow spectra at three different epochs. The best fit model consists of a standard forward shock in a wind environment (solid line), and a black body component (dashed line). The best fit parameters are $E_{k,iso} = 10^{53} \text{ erg}$, $A_* = 3.6 \times 10^{-3}$, $\epsilon_e = 0.16$, $\epsilon_B = 0.33$, $p = 2.25$. The light curves in the 0.3-3 keV and 3-10 keV bands are presented in the inset.

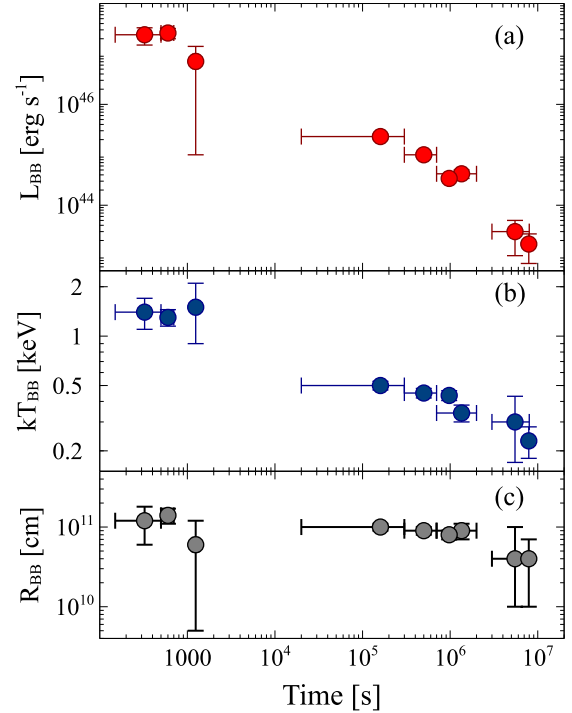


Figure 3. Parameters of the Black body component. Luminosity (a), temperature (b) and radius of the emission region (c).

$r_{ph} \approx 10^{11} \text{ cm}$ requires $\Gamma_2 \approx 0.5 \eta_{-1}^{1/3} t_3^{-5/9}$ from a few hundreds seconds to 10^7 s . This fine coupling $\Gamma \propto L_{jet}^{1/3}$ required to keep a constant photospheric radius seems somewhat contrived, although it cannot be excluded (e.g. Fan et al. 2012).

Let us now discuss the association of the blackbody with a hot plasma cocoon. The cocoon develops in-

side the star by the interaction of the jet with the stellar layers, and eventually breaks out at the stellar surface when the jet emerges (Lazzati & Begelman 2005). Starling et al. (2012) have proposed that the black body component found in a few GRBs during the steep decay phase of the X-ray light curve can be associated, at least in one event, to a relativistically expanding hot plasma cocoon. This component is short-lived ($\lesssim 1,000$ s) and its radius is rapidly increasing with time. On the contrary, our observations exhibit a long-lasting black body emission with a constant radius, indicating that the cocoon does not expand. Thus some process must confine it as it emerges at the stellar surface. A promising mechanism is magnetic confinement (Komissarov 1999). For instance, the toroidal component of the magnetic field could be advected into the inner part of the cocoon (Levinson & Begelman 2013), suppressing the plasma expansion across the magnetic field lines and confining it around the jet. In this scenario, the transverse size of the cocoon when it emerges at the stellar surface should be similar to the jet opening angle, $\theta_c \approx \theta_j \approx R_{BB}/R_*$, where R_* is the radius of the progenitor star. The limit on the jet opening angle derived previously implies $R_* \lesssim 3 \times 10^{12}$ cm, consistent with the typical radii of a BSG producing an accretion disk after the collapse (Woosley & Heger 2012; Kashiyama et al. 2013). The energy of the baryons entrained in the cocoon can be derived as $E_{th,b} \approx 3M_c/2m_p kT \approx 3 \times 10^{47}$ erg. Here M_c is the stellar mass contained within the volume excavated by the jet, that is $V_c \sim \pi R_{BB}^2 R_* \approx 10^{35}$ cm³. This energy is several orders of magnitudes lower than the energy of the accretion-powered jet, $E_{jet} \approx 5 \times 10^{53} \eta_{-1}$ erg (Wong et al. 2014), thus, if the jet is Poynting-flux dominated, its magnetic field can easily confine the plasma of the cocoon.

The blackbody energetics, $E_{BB} = 1.5 \times 10^{51}$ erg, are safely below the energy produced by a jet piercing through a BSG, $E_c \approx 10^{52}$ erg (Kashiyama et al. 2013), and are much larger than the energy of the baryons computed above. The cocoon is therefore radiation dominated, and its temperature at the instant of the break out can be estimated as $kT_{BB} \lesssim (E_{BB}/V_c)^{1/4} \approx 1$ keV, consistent with that observed. The cocoon's cooling time, $t_c \approx E_{BB}/L_{BB} \lesssim 10^4$ s, is however much shorter than the duration of the thermal emission. Thus, the cocoon must be continuously energized by a fraction η_{th} of the jet energy which, as mentioned above, follows a $L_{jet} \propto t^{-5/3}$. The black body luminosity can be expressed as $L_{BB} \approx \eta_{th} L_{jet}$. In our case $\eta_{th} \approx 0.01$. The flatter decay slope of the thermal component can be accounted by a slow increase of η_{th} when the jet energy decreases.

4. CONCLUSIONS

We conclude that the features observed in this GRB (its extremely long duration, the thermal X-ray spectrum, and the low density wind environment) are associated with a low metallicity BSG progenitor, and could characterize the class of ultralong GRBs as a whole. The fallback of the stellar outer layers supports a long duration jet, which entrains a large mass of baryons in a hot cocoon. This mass is larger than that available for a WR star, the proposed progenitor of long GRBs. Due to the larger baryon loading, it is likely that the jet Lorentz

factor at the surface of the BSG is substantially lower than the equivalent for a WR progenitor, eventually favoring a larger efficiency η_{th} . Both these effects boost the emission from the thermal cocoon in ultra-long GRBs as opposed to the case of standard long GRBs. With a typical rest-frame temperature of $kT_{BB} \sim 0.5$ keV the thermal component could not be detected in the other three presently known ultralong GRBs, all lying at larger z .

Pop III star are expected to end their life as BSG (Woosley et al. 2002; Nakauchi et al. 2012), thus their explosions should be characterized by features similar to those observed in this ultralong GRB. Pop III stars are first formed in the early universe where the low value of the metallicity ($Z < Z_{cr} \approx 10^{-4}$) favors the formation of large ($> 100 M_\odot$) collapsing gas clouds. Chemical enrichment following the first stars explosions proceed inhomogeneously, thus Population III stars can continue to form until late epochs, provided that gas pockets of sufficiently low metallicity can be preserved during cosmic evolution. Could the progenitor of GRB130925A be a rare Pop III star? Various authors (e.g. Tornatore et al. 2007) have shown that a sizeable fraction of Pop III stars can form down to $z \approx 2.5$ and, possibly, this formation could extend into the local Universe. The mass loss rate derived from the afterglow fit is suggestive of a metal-poor star. However, it cannot lead to quantitative measurements, as the mass loss is not uniquely dependent upon metallicity. The low redshift and the high dust content of the host galaxy represent an environment more typical of a Population II star, although only deep spectroscopic observations of the GRB birthsite may ultimately elucidate the nature of the progenitor.

5. ACKNOWLEDGEMENTS

We acknowledge useful discussion with A. Chieffi, C. Macculi and R. Salvaterra. We thank the XMM team for the support in carrying out the TOO observation.

REFERENCES

- Abel, T., Bryan, G. L., & Norman, M. L. 2002, *Science*, 295, 93
- Abramowicz, M. A., Novikov, I. D., & Paczynski, B. 1991, *ApJ*, 369, 175
- Arnaud, K. A. 1996, in *Astronomical Society of the Pacific Conference Series*, Vol. 101, *Astronomical Data Analysis Software and Systems V*, ed. G. H. Jacoby & J. Barnes, 17
- Bannister, K., Hancock, P., Kulkarni, S., Horesh, A., Zauderer, A., Murphy, T., & Gaensler, B. 2013, *The Astronomer's Telegram*, 5531, 1
- Barkana, R. & Loeb, A. 2001, *Phys. Rep.*, 349, 125
- Bellm, E. C., et al. 2014, *ApJ*, 784, L19
- Bromm, V., Coppi, P. S., & Larson, R. B. 2002, *ApJ*, 564, 23
- Campana, S., et al. 2006, *Nature*, 442, 1008
- de Pasquale, M., et al. 2006, *A&A*, 455, 813
- Ensmann, L. & Burrows, A. 1992, *ApJ*, 393, 742
- Evans, P. A., et al. 2009, *MNRAS*, 397, 1177
- Evans, P. A., et al. 2014, *ArXiv e-prints*
- Fan, Y.-Z., Wei, D.-M., Zhang, F.-W., & Zhang, B.-B. 2012, *ApJ*, 755, L6
- Fitzpatrick, G. 2013, *GRB Coordinates Network*, 15255, 1
- Friis, M. & Watson, D. 2013, *ApJ*, 771, 15
- Gehrels, N., et al. 2004, *ApJ*, 611, 1005
- Gendre, B., et al. 2013, *ApJ*, 766, 30
- Golenetskii, S., Aptekar, R., Frederiks, D., Pal'Shin, V., Oleynik, P., Ulanov, M., Svinkin, D., & Cline, T. 2013, *GRB Coordinates Network*, 15260, 1
- Granot, J. & Sari, R. 2002, *ApJ*, 568, 820
- Heger, A., Fryer, C. L., Woosley, S. E., Langer, N., & Hartmann, D. H. 2003, *ApJ*, 591, 288

- Kashiyama, K., Nakauchi, D., Suwa, Y., Yajima, H., & Nakamura, T. 2013, *ApJ*, 770, 8
- Komissarov, S. S. 1999, *MNRAS*, 308, 1069
- Kouveliotou, C., Meegan, C. A., Fishman, G. J., Bhat, N. P., Briggs, M. S., Koshut, T. M., Paciesas, W. S., & Pendleton, G. N. 1993, *ApJ*, 413, L101
- Kudritzki, R. P. 2002, *ApJ*, 577, 389
- Kumar, P., Narayan, R., & Johnson, J. L. 2008, *MNRAS*, 388, 1729
- Lazzati, D. & Begelman, M. C. 2005, *ApJ*, 629, 903
- Levan, A. J., et al. 2014, *ApJ*, 781, 13
- Levinson, A. & Begelman, M. C. 2013, *ApJ*, 764, 148
- Mészáros, P. & Rees, M. J. 2010, *ApJ*, 715, 967
- Nakauchi, D., Suwa, Y., Sakamoto, T., Kashiyama, K., & Nakamura, T. 2012, *ApJ*, 759, 128
- Pe'er, A., Zhang, B.-B., Ryde, F., McGlynn, S., Zhang, B., Preece, R. D., & Kouveliotou, C. 2012, *MNRAS*, 420, 468
- Quataert, E. & Kasen, D. 2012, *MNRAS*, 419, L1
- Ryde, F. & Pe'er, A. 2009, *ApJ*, 702, 1211
- Sault, R. J., Teuben, P. J., & Wright, M. C. H. 1995, in *Astronomical Society of the Pacific Conference Series*, Vol. 77, *Astronomical Data Analysis Software and Systems IV*, ed. R. A. Shaw, H. E. Payne, & J. J. E. Hayes, 433
- Savchenko, V., et al. 2013, *GRB Coordinates Network*, 15259, 1
- Sparre, M. & Starling, R. L. C. 2012, *MNRAS*, 427, 2965
- Starling, R. L. C., Page, K. L., Pe'er, A., Beardmore, A. P., & Osborne, J. P. 2012, *MNRAS*, 427, 2950
- Sudilovsky, V., Kann, D. A., & Greiner, J. 2013, *GRB Coordinates Network*, 15247, 1
- Suwa, Y. & Ioka, K. 2011, *ApJ*, 726, 107
- Tanvir, N. R., Levan, A. J., Hounsell, R., Fruchter, A. S., Cenko, S. B., Perley, D. A., & O'Brien, P. T. 2013, *GRB Coordinates Network*, 15489, 1
- Tornatore, L., Ferrara, A., & Schneider, R. 2007, *MNRAS*, 382, 945
- Vink, J. S., de Koter, A., & Lamers, H. J. G. L. M. 2001, *A&A*, 369, 574
- Vreeswijk, P. M., Malesani, D., Fynbo, J. P. U., De Cia, A., & Ledoux, C. 2013, *GRB Coordinates Network*, 15249, 1
- Willingale, R., et al. 2007, *ApJ*, 662, 1093
- Wong, T.-W., Fryer, C. L., Ellinger, C. I., Rockefeller, G., & Kalogera, V. 2014, *ArXiv e-prints*
- Woosley, S. E. & Bloom, J. S. 2006, *ARA&A*, 44, 507
- Woosley, S. E. & Heger, A. 2012, *ApJ*, 752, 32
- Woosley, S. E., Heger, A., & Weaver, T. A. 2002, *Reviews of Modern Physics*, 74, 1015